CoS Acicular Nanorod Arrays for the Counter Electrode of an Efficient Dye-Sensitized Solar Cell

Chung-Wei Kung,[†] Hsin-Wei Chen,[†] Chia-Yu Lin,[†] Kuan-Chieh Huang,[†] R. Vittal,[†] and Kuo-Chuan Ho[†,‡,*]

[†]Department of Chemical Engineering and [‡]Institute of Polymer Science and Engineering, National Taiwan University, Taipei 10617, Taiwan

ABSTRACT

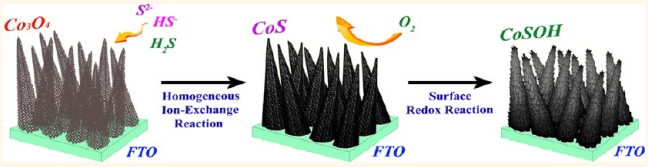

One-dimensional cobalt sulfide (CoS) acicular nanorod arrays (ANRAs) were obtained on a fluorine-doped tin oxide (FTO) substrate by a two-step approach. First, Co_3O_4 ANRAs were synthesized, and then they were converted to CoS ANRAs for various periods. The compositions of the films obtained after various conversion periods were verified by X-ray diffraction, UV−visible spectrophotometry, and X-ray photoelectron spectroscopy; their morphologies were examined at different periods by scanning electron microscopic and transmission electron microscopic images. Electrocatalytic abilities of the films toward I^-/I_3^- were verified through cyclic voltammetry (CV) and Tafel polarization curves. Long-term stability of the films in I^-/I_3^- electrolyte was studied by CV. The FTO substrates with CoS ANRAs were used as the counter electrodes for dye-sensitized solar cells; a maximum power conversion efficiency of 7.67% was achieved for a cell with CoS ANRAs, under 100 mW/cm^2, which is nearly the same as that of a cell with a sputtered Pt counter electrode (7.70%). Electrochemical impedance spectroscopy was used to substantiate the photovoltaic parameters.

KEYWORDS: acicular nanorods · cobalt oxide · cobalt sulfide · counter electrode · dye-sensitized solar cell

Nanoscale materials have been known to show superior properties for applications in several fields, compared to their corresponding bulk materials.[1] Among different kinds of nanoscale morphologies, one-dimensional (1D) nanostructure arrays of solids attract wide interest because of their excellent technological advantages in electronics, optoelectronics, and memory devices.[2] In addition, 1D nanostructure arrays are known to be beneficial for electronic conduction along the axial direction through the arrays to their substrate.[3,4] In order to fabricate 1D nanostructure arrays of the materials which cannot grow in 1D direction directly, some solid template-assisted methods were applied.[5−8] These methods typically include three steps: the first step for synthesizing the 1D nanostructure arrays of the template material on the substrate, the second step for coating the target material on the template, and the third step for removing the template and obtaining the required 1D nanostructure. Among several template materials, anodic aluminum oxide (AAO) is the most common and successful one used for the synthesis of 1D nanostructure arrays. However, the synthesis by using AAO is associated with several inconveniences, especially the removal of the template to obtain robust nanostructure arrays without any structural variation.[9] Another alternative approach to prepare 1D nanostructure arrays is the direct conversion of the 1D arrays of the precursor material on the substrate to the 1D arrays of the target material. For instance, Li *et al.* applied this strategy to prepare CdS or CdSe microtube arrays by converting CdOHCl microrod arrays to them on a glass substrate directly; this method has several advantages, with reference to the method using AAO.[10] However, research on the construction of 1D nanostructures or microstructure arrays by using this strategy is at a low profile.

Cobalt sulfides are known to show a variety of chemical formulas (*e.g.*, Co_9S_8, CoS, Co_3S_4, Co_4S_3, and CoS_2).[11] Among these compounds, Co_9S_8 has been studied for its role in the hydrodesulfurization catalyst.[11] In recent years, cobalt sulfides have been also proposed for the electrochemical capacitors[12−14] and for the cathodes of lithium batteries,[15] due to their excellent electrocatalytic ability. In order to further enhance the electrocatalytic ability of cobalt sulfide, its nanostructures with various morphologies were synthesized, such as three-dimensional (3D) nanospheres[13,15] and two-dimensional (2D) nanoflakes.[14,16] Research on the synthesis of 1D nanostructures of cobalt sulfides is still insufficient due to the difficulty of growing cobalt sulfides in the 1D direction directly.[17] Chen *et al.* synthesized the powder of 1D Co_3S_4 nanotubes by converting the

* Address correspondence to kcho@ntu.edu.tw.

Received for review May 10, 2012 and accepted July 2, 2012.

Published online July 02, 2012
10.1021/nn302063s

© 2012 American Chemical Society

powder of $Co(CO_3)_{0.35}Cl_{0.20}(OH)_{1.10}$ nanowires to it.[18] Bao *et al.* developed a biomolecule-assisted method to synthesize a powder of CoS nanowires on a Ni substrate by using some organic binders.[12] The powder of Co_9S_8 nanotubes was synthesized by Wang *et al.* by using $Co(CO_3)_{0.35}Cl_{0.20}(OH)_{1.10}$ nanorods as the template.[17] However, only powders of 1D nanostructures of cobalt sulfides were prepared in the mentioned literatures, that is to say, they were not in the form of a thin film and it was not viable to arrange or deposit them on a substrate in a regular fashion. CoS_2 nanowire arrays were, however, prepared by Yue *et al.* by using AAO.[7,19]

Dye-sensitized solar cells (DSSCs) have in recent years attracted great attention from researchers all over the world for their inherence of low cost, easy fabrication, and relatively high efficiency for the conversion of sunlight into electricity.[20,21] Basically, a DSSC consists of a photoanode with titanium dioxide, adsorbed with a photosensitizing dye, a redox electrolyte, and a counter electrode (CE). CE is not only an essential part of a DSSC but also an important component in determining its performance. A platinum-sputtered (s-Pt) conducting glass is usually employed as the CE for a DSSC. However, platinum is very expensive and is rare on earth. Fabrication of CEs with other cheaper materials is expected to bring down the production cost of the cells, especially when it is a matter of large-scale production. Several materials, including carbon materials[22,23] and conducting polymers,[24] have been used to fabricate platinum-free CEs for DSSCs. In recent years, CoS has been proposed for the CE of DSSCs due to its excellent catalytic ability toward I_3^- and its low cost.[25] The performance of the cell with CoS is comparable to that of the cell with platinum, and this indicates the high potential of CoS to replace platinum for the CE of a DSSC.

In this study, novel 1D CoS acicular nanorod arrays (ANRAs) were prepared by a two-step approach. The Co_3O_4 ANRAs were deposited first on a conducting fluorine-doped tin oxide (FTO) substrate and then were converted to CoS directly by a simple chemical bath process. To the best of our knowledge, this is the first time that 1D nanostructure arrays of cobalt sulfides have been prepared directly on a conducting substrate, that is, in the absence of a template such as AAO. This study thus provides a breakthrough in the nanoscale syntheses of cobalt sulfides. This is also the first report on the use of a CE with 1D nanostructure of cobalt sulfides for a DSSC. The novel 1D CoS ANRAs were applied for the counter electrodes of DSSCs; one of the DSSCs with these CoS ANRAs shows a high efficiency of 7.67%, under 100 mW/cm^2, which is nearly the same as that of a DSSC with Pt as its CE (7.70%).

RESULTS AND DISCUSSION

Characterization of the Films. *X-ray Diffraction Patterns.* Figure 1 shows X-ray diffraction (XRD) patterns of the thin film of Co_3O_4 ANRAs and the thin films of CoS ANRAs, obtained after various conversion periods. As revealed in pattern (i) in Figure 1, all of the diffraction peaks of the Co_3O_4 ANRAs film before the conversion process can be indexed to Co_3O_4, according to Joint Committee on Powder Diffraction Standards (JCPDS, PDF no. 80-1545). The diffraction pattern of the Co_3O_4 ANRAs film after 3 h of conversion period shows still minute remains of the peaks of Co_3O_4, indicating that the conversion to well-crystalline CoS has not yet begun; however, for the sake of explanations, we still designate this film as CoS ANRAs-3h. In the XRD pattern of the CoS ANRAs film obtained after 12 h of conversion (CoS ANRAs-12h), only the diffraction peaks of CoS can be observed, according to JCPDS, PDF no. 75-0605. The peak positions (degrees) and peak intensities of the XRD pattern of the CoS ANRAs film obtained after 24 h of conversion (CoS ANRAs-24h) are the same as those of the XRD pattern of the CoS ANRAs-12h. In the XRD pattern of the CoS ANRAs film obtained after 36 h of conversion (CoS ANRAs-36h), the diffraction peaks of CoS can still be observed, but the peak intensities show considerable decrease; the possible reason for this observation is the formation of some amorphous substance on the film surface of CoS ANRAs-36h.

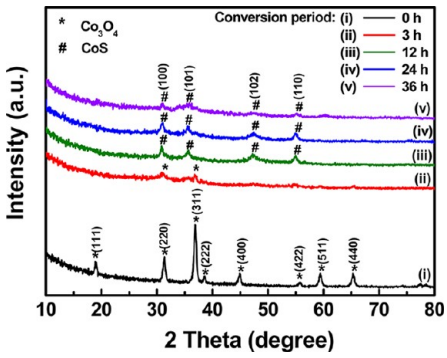

Figure 1. XRD patterns of the thin films of ANRAs obtained after various conversion periods: (i) 0 h (Co_3O_4 ANRAs), (ii) 3 h, (iii) 12 h, (iv) 24 h, and (v) 36 h.

Morphological Characterization. The scanning electron microscopic (SEM) images of the films of Co_3O_4 ANRAs, CoS ANRAs-3h, CoS ANRAs-12h, CoS ANRAs-24h, and CoS ANRAs-36h are shown in Figure 2a–e, respectively. From Figure 2a, it can be seen that the Co_3O_4 film before the conversion has 1D acicular nanorod arrays, with relatively smooth surface of the nanorods. After 3 h of the conversion process, the 1D acicular morphology remains the same, but the surface of each nanorod becomes rougher, as shown in Figure 2b. Figure 2c shows the surface morphology of CoS ANRAs-12h, which is almost the same as that of CoS ANRAs-3h. The surface morphology of CoS ANRAs-24h is shown in Figure 2d. The surface of each nanorod in Figure 2d is much rougher and shows several flake-like nanostructures. The surface morphology of CoS ANRAs-36h is shown in Figure 2e; several large

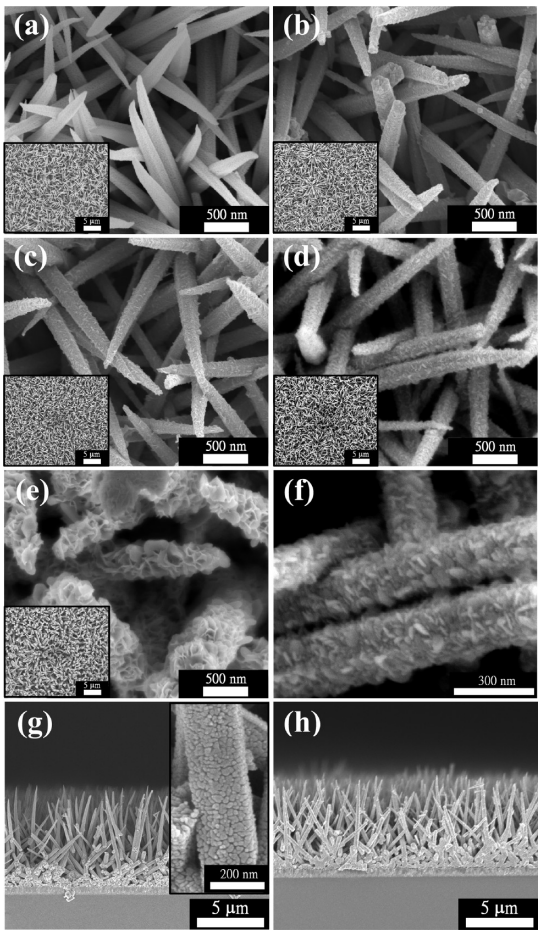

Figure 2. SEM images of the films of (a) Co_3O_4 ANRAs, (b) CoS ANRAs-3h, (c) CoS ANRAs-12h, (d) CoS ANRAs-24h, (e) CoS ANRAs-36h, (f) CoS ANRAs-24h, at high magnification, (g) Co_3O_4 ANRAs at cross section, and (h) CoS ANRAs-24h at cross section. The insets of (a−e) show the large-scale SEM images of the corresponding ANRAs, and the inset of (g) shows a single nanorod of the Co_3O_4 ANRAs.

nanoflakes are arranged densely, and they cover the full surface of each nanorod; this morphology is quite different from those of others. A small-scale SEM image of CoS ANRAs-24h is shown in Figure 2f; the surface of the nanorods of CoS ANRAs-24h is composed of several tiny nanoflakes. The insets of Figure 2a−e show the large-scale SEM images of the corresponding ANRAs. These insets in Figure 2a−e show that all nanorods of the films, obtained at different conversion periods, are arranged uniformly, and they cover the full surface of their substrates; this observation indicates that the conversion process does not damage the basic morphology of the 1D nanorod arrays. The cross-sectional SEM images of the films of Co_3O_4 ANRAs and CoS ANRAs-24h are shown in Figure 2g,h, respectively. From these two images (Figure 2g,h), the thicknesses of both films could be estimated to be about 7 μm. Figure 2g,h shows that the acicular nanorods are arranged uniformly in an array form, and the adhesion between the ANRAs and the substrate is strong. The inset of Figure 2g shows a single rod of the Co_3O_4 ANRAs. While the surface of a single nanorod of CoS ANRAs-24h (Figure 2f) shows tiny nanoflakes, the surface of the single nanorod of Co_3O_4 ANRAs (inset of Figure 2g) shows tiny spherical or elliptical nanoparticles.

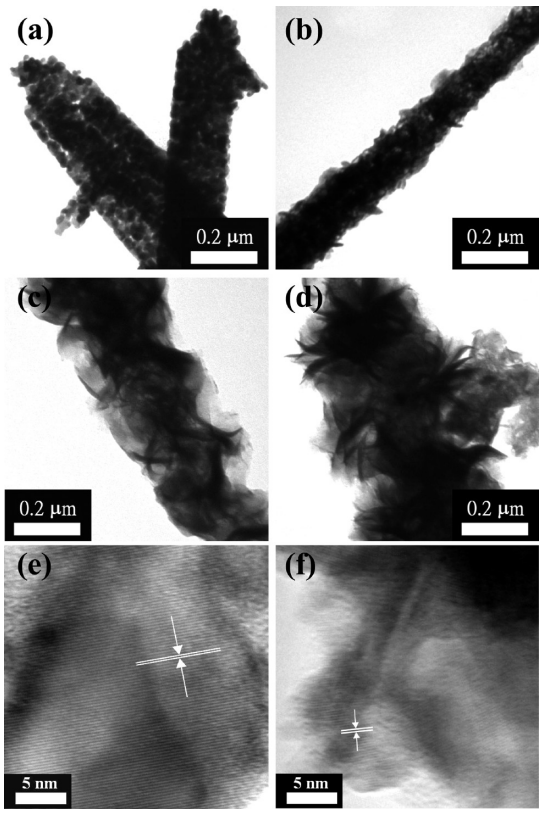

Figure 3. TEM images of the nanorods scraped from the films of (a) Co_3O_4 ANRAs, (b) CoS ANRAs-12h, (c) CoS ANRAs-24h, and (d) CoS ANRAs-36h; HRTEM images of a single nanorod scraped from the films of (e) Co_3O_4 ANRAs and (f) CoS ANRAs-24h.

Figure 3a−d shows the transmission electron microscopic (TEM) images of the nanorods scraped from the films of Co_3O_4 ANRAs, CoS ANRAs-12h, CoS ANRAs-24h, and CoS ANRAs-36h, respectively. From Figure 3a, it can be seen that the Co_3O_4 nanorods possess a highly porous nanostructure, composed of several tiny spherical or elliptical nanoparticles. This observation agrees with that of the SEM image in the inset of Figure 2g, which also shows a nanorod of Co_3O_4. After 12 h of the conversion process, the nanorod becomes much denser inside, with a rougher surface outside, as shown in Figure 3b. Figure 3c shows the TEM image of a nanorod from CoS ANRAs-24h; the nanorod has several nanoflakes in it (compare with Figure 2f). After 36 h of conversion, as shown in Figure 3d, the nanorod shows several large and mosaic flower-like nanoflakes on its surface (compare with Figure 2e). After various periods of conversion (Figure 3b−d), it should be noted that all of the CoS nanorods are solid instead of hollow, implying that the conversion process is homogeneous and reaction-controlled. This observation

can be explained by the highly porous Co_3O_4 nanorod used for the conversion process (Figure 3a), which is beneficial for the facile diffusion of S^{2-} or HS^- into the core of the nanorod of Co_3O_4 during the conversion process. The films of Co_3O_4 ANRAs and CoS ANRAs-24h were subjected to further investigation using high-resolution transmission electron microscopy (HRTEM). HRTEM images of single nanorods of Co_3O_4 ANRAs and CoS ANRAs-24h (scraped from the corresponding films) are shown in Figure 3e,f, respectively. The image in Figure 3e indicates a lattice spacing of 2.476 Å; this can be ascribed to the (311) planar spacing of Co_3O_4 (PDF no. 80-1545). The estimated value of the lattice spacing in the case of CoS ANRAs-24h is 2.818 Å, which can be ascribed to the (100) planar spacing of CoS (PDF no. 75-0605). The results of HRTEM agree well with the XRD patterns in Figure 1.

Single nanorods of Co_3O_4 ANRAs and CoS ANRAs-12h were further investigated by TEM along with energy-dispersive spectroscopy (EDS) mapping, and the results are shown in Figures S1 and S2 in the Supporting Information. Figure S1 shows that the porous nanorod of Co_3O_4 ANRAs consists of uniformly distributed Co and O; Figure S2 shows that the nanorod of CoS ANRAs-12h consists of Co and S. It can be seen in Figure S2 that the mapping points of Co and S are uniformly distributed in the nanorod; this indicates that the nanorod is in the solid form and not in the hollow form. Furthermore, only the background points of oxygen can be seen in the mapping result of CoS ANRAs-12h (Figure S2c); this shows that Co_3O_4 was completely converted to CoS after 12 h.

UV–Visible Spectra and X-ray Photoelectron Spectroscopy. In order to confirm the compositions of the nanorods obtained after various periods of conversion, they were scraped from their films, their suspensions were obtained in ethanol, and their UV–visible spectra were obtained; the spectra are shown in Figure 4a. Three broad absorption peaks with their centers located at about 260, 480, and 760 nm can be observed in the UV–visible spectrum of Co_3O_4 ANRAs. These three broad peaks agree with the characteristic UV–visible absorption peaks of Co_3O_4.[26] Despite some shifts, the broad peaks at 480 and 760 nm still remain in the spectrum of CoS ANRAs-3h; however, two new peaks can be observed in this spectrum, located at 215 and 270 nm. This result indicates the incomplete conversion of Co_3O_4 to CoS ANRAs after 3 h. Similar absorption behaviors are observed in the cases of CoS ANRAs-12h, CoS ANRAs-24h, and CoS ANRAs-36h. The characteristic peaks of Co_3O_4 do not appear in these three spectra; only the peaks at 215 and 270 nm corresponding to CoS can be seen in these spectra. The results of UV–visible spectra confirm that the Co_3O_4 ANRAs film could be completely converted to the film of CoS after the conversion periods of more than 12 h. UV–vis spectra measured by UV–vis diffuse

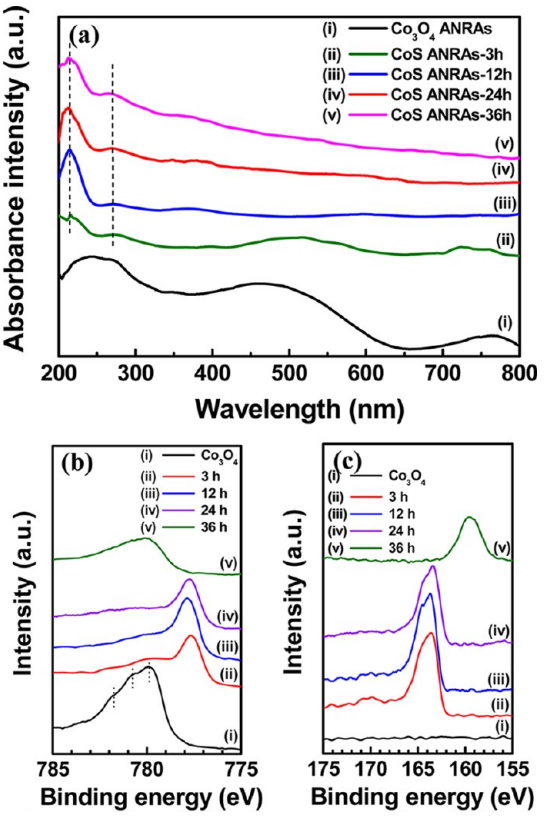

Figure 4. (a) UV–visible absorption spectra of the suspensions obtained from the scraps of the films of (i) Co_3O_4 ANRAs, (ii) CoS ANRAs-3h, (iii) CoS ANRAs-12h, (iv) CoS ANRAs-24h, and (v) CoS ANRAs-36h; XPS spectra in the regions of (b) Co $2p_{3/2}$ and (c) S 2p for the films mentioned above.

reflectance spectroscopy were also obtained for the films of Co_3O_4 and CoS to verify the results of UV–vis absorption spectra in Figure 4a; the spectra are shown in Figure S3 in the Supporting Information. A detailed discussion is made in this regard in the Supporting Information.

X-ray photoelectron spectroscopy (XPS) analysis was applied to further verify the surface compositions of the film of Co_3O_4 ANRAs and the films of CoS ANRAs obtained after various periods of conversion; high-resolution XPS spectra of the films, obtained for the regions of Co $2p_{3/2}$ and S 2p are shown in Figure 4b,c, respectively. In the case of Co_3O_4 ANRAs film, three overlapped peaks can be observed for the spectrum of the film in the region of Co $2p_{3/2}$, with the centers of 779.9, 780.8, and 781.8 eV. These three peaks correspond to Co_3O_4, CoOOH, and $Co(OH)_2$, respectively.[27,28] The peak at 779.9 eV shows the largest enclosed area, which indicates that the major phase of the film is Co_3O_4. No peak can be observed for the spectrum of Co_3O_4 ANRAs in the region of S 2p. This indicates that the Co_3O_4 film does not contain any sulfide. The XPS spectra of CoS ANRAs-3h, CoS ANRAs-12h, and CoS ANRAs-24h show the same patterns for both the regions of Co $2p_{3/2}$ and S 2p. Three peaks for CoS ANRAs-3h, CoS

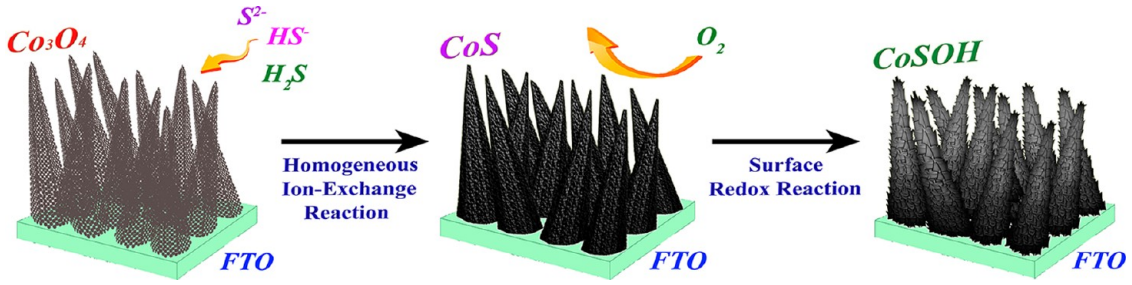

Scheme 1. Mechanism of the conversion process from Co_3O_4 ANRAs to CoS ANRAs and then to CoSOH.

ANRAs-12h, and CoS ANRAs-24h can be observed at 777.8 eV in the region of Co $2p_{3/2}$, and three peaks for the same can be observed at 163.5 eV in the region of S 2p; in both of these regions, the peaks agree well with XPS spectral characteristics of CoS reported in the literature.[29−31] The film of CoS ANRAs-36h shows quite different XPS spectra in the regions of Co $2p_{3/2}$ and S 2p, that is, a broad Co $2p_{3/2}$ peak at the center of 780.2 eV and a S 2p peak at 159.7 eV. The Co $2p_{3/2}$ peak for CoS ANRAs-36h agrees with the Co $2p_{3/2}$ peak for CoSOH reported previously;[32] however, the S 2p peak for CoS ANRAs-36h shifts, with respect to the S 2p peak of CoSOH reported in this work, in which the S 2p peak appears at about 162.5 eV. In the absence of any other report in this regard and because of the agreement in the location of Co $2p_{3/2}$, we assume that the peak in our case at 159.7 eV is due to CoSOH.[32] In the presence of oxygen, CoSOH is known to be oxidized from CoS in the alkaline solution used for the conversion process.[14] CoSOH may be the major composition of the large and mosaic flower-like nanoflakes of CoS ANRAs-36h observed in the SEM and TEM images. CoSOH may be amorphous on the surface of the nanorods and may be the root cause for the decrease in the intensities of XRD peaks of CoS ANRAs-36h. A possible mechanism is proposed for the conversion process and is shown in Scheme 1. In the aqueous solution, Na_2S dissolves to form S^{2-} ions and is also hydrolyzed to generate HS^- and H_2S species.[17,33] All of these species can serve as the sulfur sources for the ion-exchange reaction to convert Co_3O_4 to CoS. The porous Co_3O_4 ANRAs allow these sulfur sources to diffuse easily into the core of each nanorod. Thus, the reaction occurs relatively slow, as compared to the diffusion, to convert all of the Co_3O_4 ANRAs to CoS ANRAs homogeneously. Thereafter, due to the presence of oxygen, the surface redox reaction takes place on the surface of each CoS nanorod. The CoS on the surface is oxidized by oxygen to form CoSOH. Thus, at the conversion period of 36 h, the large and mosaic flower-like nanoflakes of CoSOH, which are obtained due to the conversion of CoS, would cover the full surface of the CoS nanorods.

Electrocatalytic Abilities of the Counter Electrodes toward I^-/I_3^- Redox Couple. Electrocatalytic abilities of the CEs with the films of Co_3O_4 ANRAs, CoS ANRAs-3h, CoS ANRAs-12h, CoS ANRAs-24h, CoS ANRAs-36h, and sputtered Pt were

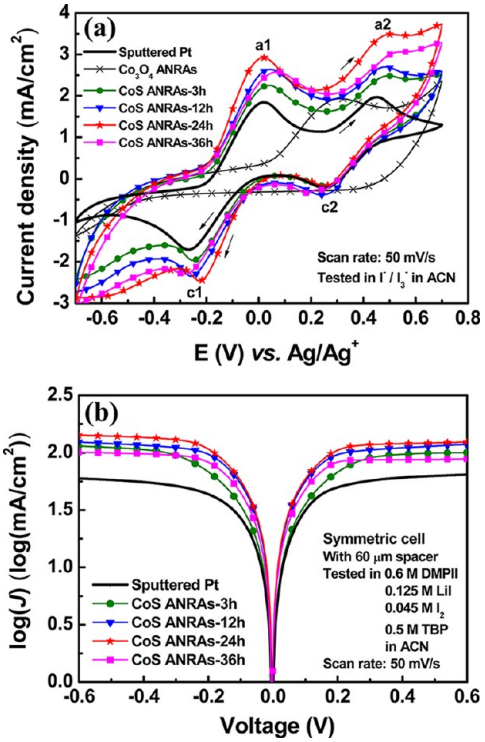

Figure 5. (a) CV curves of the CEs with the films of Co_3O_4 ANRAs, CoS ANRAs-3h, CoS ANRAs-12h, CoS ANRAs-24h, CoS ANRAs-36h, and sputtered Pt, obtained in ACN solution containing 10.0 mM LiI, 1.0 mM I_2, and 0.1 M $LiClO_4$, at a scan rate of 50 mV/s. (b) Tafel polarization curves of these CEs, obtained by using symmetrical cells with two identical electrodes in the same electrolyte as that used in DSSCs at the scan rate of 50 mV/s.

studied by cyclic voltammetry (CV), performed as explained in the Methods section. The obtained CV curves of the CEs are shown in Figure 5a. The CVs were scanned from −0.7 V. It can be seen in Figure 5a that each of the CV curves, except that for Co_3O_4 ANRAs, shows two pairs of redox peaks. The redox peaks at more negative potentials, represented by a1 and c1, correspond to the reaction of eq 1, and the redox peaks at more positive potentials, represented by a2 and c2, correspond to eq 2[34]

$$3I^- \leftrightarrow I_3^- + 2e^- \quad (1)$$

$$2I_3^- \leftrightarrow 3I_2 + 2e^- \quad (2)$$

The electrocatalytic ability of a CE for I_3^- reduction in a DSSC can be visualized in terms of its cathodic peak

current (I_{pc}) at more negative potential, that is, at c1 in this case, related to the reaction shown in eq 1.[34] The magnitude of this cathodic peak current density at c1 indicates the electrocatalytic ability of the pertinent counter electrode for the reduction of I_3^- ions in the corresponding DSSC. From Figure 5a, it can be seen that the CV curve of the CE with Co_3O_4 ANRAs shows a quite different behavior compared to other CV curves; this CV curve does not show any redox peaks at more negative potentials, implying the poor electrocatalytic ability of Co_3O_4 ANRAs toward I_3^-. The CV curves of the CEs with CoS ANRAs-3h, CoS ANRAs-12h, CoS ANRAs-24h, CoS ANRAs-36h, and with the sputtered Pt show two pairs of redox peaks, indicating that they all have electrocatalytic ability for the reduction of triiodide ions. It should be noted that all of the CoS ANRAs show higher anodic and cathodic peak current densities than those of sputtered Pt. This observation implies that the electrocatalytic ability of CoS toward the I^-/I_3^- redox couple is better than that of Pt. Moreover, among the four CEs with CoS ANRAs, the CE with CoS ANRAs-3h shows the least peak current density at c1; this may be attributed to incomplete conversion of Co_3O_4 to CoS for the period of 3 h. The CE with CoS ANRAs-24h shows the highest peak current density among all, indicating that 24 h is the optimal period for the conversion process; in other words, the electrocatalytic ability of CoS ANRAs-24h is the best among all and is even better than that of Pt. The CV curve of the CE with CoS ANRAs-36h shows a smaller peak current density at c1, compared to that of the CE with CoS ANRAs-24h. The amorphous flower-like nanoflakes of CoSOH on the surfaces of the nanorods of CoS obtained after 36 h may act as a resistive layer for the reduction of triiodide ions and may thus be a reason for this poorer electrocatalytic ability of CoS ANRAs-36h.

Tafel polarization curves are usually used to study the electrocatalytic abilities of CEs for DSSCs.[25,35] In order to verify the electrocatalytic abilities of the CEs with sputtered Pt and with different films of CoS ANRAs, their Tafel polarization curves were obtained using symmetrical cells. The electrolyte used for the symmetrical cells was the same as that used for the DSSCs; 60 μm thick Surlyn was used as the spacer, which was the same as that used for the DSSCs. The Tafel polarization curves are shown in Figure 5b. The exchange current density (J_0), which is directly related to the electrocatalytic ability of an electrode, can be estimated from the extrapolated intercepts of the anodic and cathodic branches of the corresponding Tafel curves.[36] From Figure 5b, it can be seen that the CE with CoS ANRAs-24h shows the highest J_0 among all, and the tendency of the J_0 totally agrees with the tendency of the peak current density observed in Figure 5a. It should be noted in Figure 5b that the exchange current densities of all CEs with CoS are much larger than that of sputtered Pt-CE; this observation may be attributed to the much higher surface

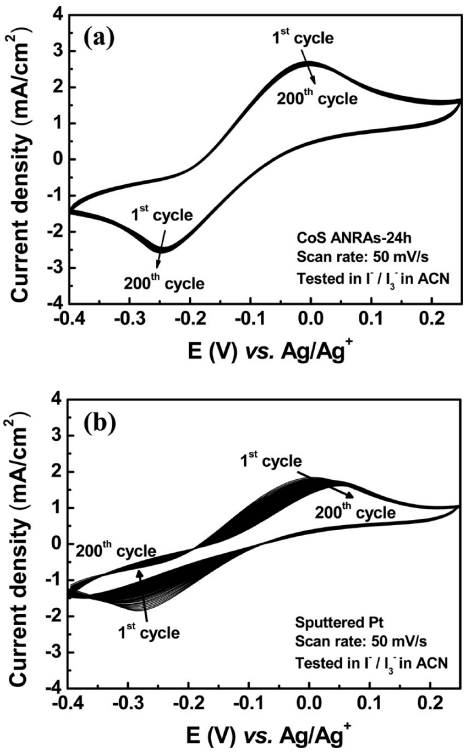

Figure 6. (a) CV curves of the CE with CoS ANRAs-24h, obtained for 200 cycles, and (b) CV curves of the CE with the sputtered Pt, obtained for 200 cycles. The CVs were obtained in the electrolyte containing 10.0 mM LiI, 1.0 mM I_2, and 0.1 M $LiClO_4$ in ACN at a scan rate of 50 mV/s.

areas of CoS ANRAs, which were apparently provided by their lengthy nanorods (about 7 μm).

Long-Term Stability Test in the I^-/I_3^- Electrolyte. In order to verify that the CoS ANRAs are reliable materials to replace sputtered Pt on the CE of a DSSC, long-term stability of the CE with the film of CoS ANRAs-24h was studied in the I^-/I_3^- electrolyte, again by cyclic voltammetry, using 200 cycles of scan. The CV was obtained in the same electrolyte, containing 10.0 mM LiI, 1.0 mM I_2, and 0.1 M $LiClO_4$ in acetonitrile (ACN). The scan rate was also the same 50 mV/s, but the potential window was changed to −0.4 to 0.25 V, which includes only the redox peaks of eq 1. As the reference, the CV of the sputtered Pt-CE was also obtained. The CV curves obtained for 200 cycles for the CEs with CoS ANRAs-24h and sputtered Pt are shown in Figure 6a,b, respectively. In Figure 6a, it can be seen that there is only a slight change between the first and 200th CV curves of the CE with CoS ANRAs-24h. The CV curve after 200 cycles of scan shows a 7% increase in the cathodic peak current density and a 5% decrease in the anodic peak current density, indicating that the electrode becomes more beneficial for the electrocatalytic reduction of I_3^-. However, the CV curves of the sputtered Pt-CE show a significant difference between the first cycle and the 200th cycle, as shown in Figure 6b. Both the anodic and cathodic peak current densities decrease dramatically after 200 cycles of scan, implying the deactivation of Pt

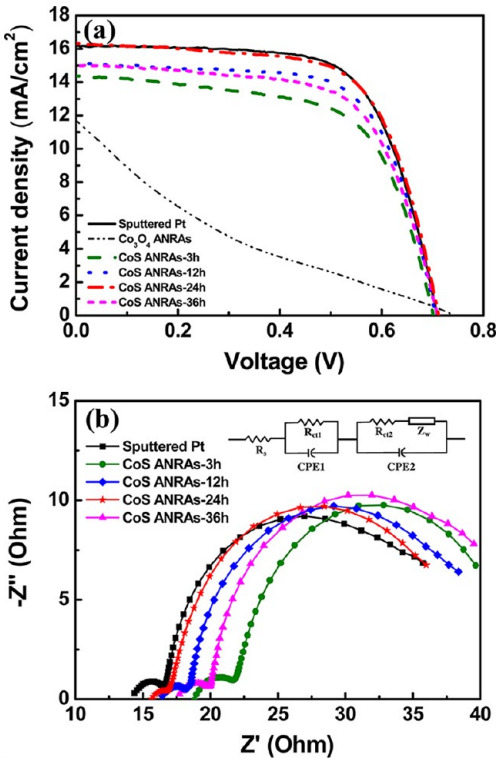

Figure 7. (a) *J*–*V* curves of the DSSCs with the films of Co_3O_4 ANRAs, CoS ANRAs-3h, CoS ANRAs-12h, CoS ANRAs-24h, CoS ANRAs-36h, and sputtered Pt measured under a light intensity of 100 mW/cm^2. (b) EIS spectra of the DSSCs mentioned above, measured under a light intensity of 100 mW/cm^2.

in I^-/I_3^- medium. The deactivation of Pt in I^-/I_3^- medium has been reported previously.[37] From Figure 6, it can be clearly seen that the CE with CoS ANRAs-24h is more stable than the CE with the sputtered Pt in I^-/I_3^- medium. Thus, it is now very clear that CoS ANRAs-24h is a reliable material to replace sputtered Pt on the CE of a DSSC.

Performance of DSSCs Using Various Counter Electrodes. Photocurrent density–voltage (*J*–*V*) curves of the DSSCs using CEs with the films of Co_3O_4 ANRAs, CoS ANRAs-3h, CoS ANRAs-12h, CoS ANRAs-24h, CoS ANRAs-36h, and sputtered Pt were obtained under a light intensity of 100 mW/cm^2, which is defined as 1 sun. The obtained *J*–*V* curves are shown in Figure 7a; the photovoltaic parameters of the DSSCs, including open-circuit voltage (V_{OC}), short-circuit current density (J_{SC}), fill factor (FF), and cell efficiency (η) are listed in Table 1. The error bars in Table 1 were estimated from the *J*–*V* curves of three separate experiments for each condition. From Figure 7a, it can be seen that the DSSC with Co_3O_4 ANRAs shows a poor cell performance, obviously due to the poor electrocatalytic ability of Co_3O_4 ANRAs for I_3^-. However the V_{OC} of the cell with Co_3O_4 ANRAs is the highest among all (Table 1). The redox potential of the triiodide/iodide couple with the Co_3O_4 electrode is different from that with the CoS electrode; such a difference varies the open-circuit voltage in a DSSC because the open-circuit voltage is the difference between the redox potential of the

TABLE 1. Photovoltaic Parameters of the DSSCs with the Films of Co_3O_4 ANRAs, CoS ANRAs-3h, CoS ANRAs-12h, CoS ANRAs-24h, CoS ANRAs-36h, and Sputtered Pt, Measured under a Light Intensity of 100 mW/cm^2

CE	V_{OC} (V)	J_{SC} (mA/cm^2)	FF	η (%)	R_{ct1} (Ω)	R_s (Ω)
Co_3O_4 ANRAs	0.74 ± 0.01	11.72 ± 0.61	0.16 ± 0.01	1.42 ± 0.10		
CoS ANRAs-3h	0.70 ± 0.01	14.37 ± 0.37	0.63 ± 0.02	6.36 ± 0.30	3.18	18.9
CoS ANRAs-12h	0.71 ± 0.01	15.11 ± 0.55	0.66 ± 0.01	7.16 ± 0.27	2.15	16.4
CoS ANRAs-24h	0.71 ± 0.01	16.31 ± 0.28	0.66 ± 0.01	7.67 ± 0.22	1.25	15.8
CoS ANRAs-36h	0.71 ± 0.01	15.00 ± 0.68	0.65 ± 0.01	6.89 ± 0.34	2.53	17.6
sputtered Pt	0.71 ± 0.01	16.17 ± 0.49	0.67 ± 0.01	7.70 ± 0.17	2.60	14.2

mediator and the Fermi level of the nanocrystalline film. Among the four DSSCs using various kinds of CoS ANRAs as their CEs, the DSSC using CoS ANRAs-3h shows the lowest J_{SC}, FF, and η, as shown in Table 1; this is to be attributed to the incomplete conversion of Co_3O_4 in CoS ANRAs-3h. The DSSC with the CE with CoS ANRAs-24h shows the best performance among all. The cell efficiency of this cell is 7.67%, which is virtually the same as that of the DSSC with the sputtered Pt-CE (7.70%, Table 1). Both the J_{SC} and FF are found to decrease for the cell with CoS ANRAs-36h, compared to those of the cell with CoS ANRAs-24h; this led to a reduced η in the case of the cell with CoS ANRAs-36h, with reference to that of the cell with CoS ANRAs-24h. These decreases may be attributed to increased resistance for electron transfer at the CE with the film of CoS ANRAs-36h, owing to the amorphous flower-like nanoflakes on the nanorods of CoS ANRAs-36h; the decreased CV currents of the three-electrode cell and J_0 of the symmetrical cell with CoS ANRAs-36h, with respect to those of such cells with CoS ANRAs-24h (Figure 5), are in agreement with this explanation of increased resistance. It should be noted that all of the DSSCs using CoS ANRAs show smaller FF values than that of the DSSC with sputtered Pt-CE. This result may be attributed to the lower conductivity of CoS compared to that of Pt.

Figure 7b shows electrochemical impedance spectra (EIS) of the DSSCs using CEs with the films of CoS ANRAs-3h, CoS ANRAs-12h, CoS ANRAs-24h, CoS ANRAs-36h, and sputtered Pt, obtained under 100 mW/cm^2; the inset shows the equivalent circuit model used for DSSCs. Each of the Nyquist plots consists of three semicircles, and they represent, from left to right, the electrocatalytic resistance at the interface between the electrolyte and the CE (R_{ct1}), the charge-transfer resistance at the interface of TiO_2/dye/electrolyte (R_{ct2}), and the Warburg diffusion resistance of I^-/I_3^- in the electrolyte (Z_w). Since a very thin spacer (Surlyn) of 60 μm was used in the DSSC, Z_w is insignificant and is not followed with interest here. From Figure 7b, it can be seen that the values of R_{ct2} are nearly the same because only CEs differ here. The values of R_{ct1} for the DSSCs with the sputtered Pt, CoS ANRAs-3h, CoS ANRAs-12h,

CoS ANRAs-24h, and CoS ANRAs-36h CEs are 2.60, 3.18, 2.15, 1.25, and 2.53 Ω, respectively (Table 1). It can be observed that the tendency of R_{ct1} agrees with the tendencies of cell efficiency and J_{SC} in Table 1, except in the case of sputtered Pt-CE. To explain this observation, the effect of the series resistance (R_s) is considered. The values of R_s for the DSSCs with the films of sputtered Pt, CoS ANRAs-3h, CoS ANRAs-12h, CoS ANRAs-24h, and CoS ANRAs-36h are 14.2, 18.9, 16.4, 15.8, and 17.6 Ω, respectively (Table 1). The tendency of R_s totally agrees with the tendencies of FF and cell efficiency listed in Table 1, indicating that the DSSC with a lower value of R_s shows a higher FF and cell efficiency. The DSSC with the sputtered Pt-CE shows the smallest R_s and highest FF and η, due to highest conductivity of Pt among all. Although the electrocatalytic ability of the sputtered Pt-CE is not the best (the corresponding R_{ct1} is not the smallest), the DSSC using sputtered Pt still shows the highest power conversion efficiency (η) among all of the DSSCs.

The efficiency of the DSSC with CoS ANRAs-24h on its CE (7.67%) is less than that obtainable with a DSSC with a TiO_2 photoanode and a platinum CE (9−11%); it is important to note that such a DSSC with Pt-CE showed only 7.7% in this study. One major reason for this less efficiency is that 60 μm thick Surlyn was used as the spacer in the fabrication of DSSCs in this work, while usually a 25 μm spacer is used in the cells with TiO_2 photoanodes and Pt-CEs. Our previous study has indicated that a DSSC with a spacer thickness of 25 μm gives a higher efficiency by about 0.8% than that of a cell with a spacer thickness of 60 μm.[38] Another reason is that we focused on the counter electrode part, giving less importance to power conversion efficiency.

The CE with CoS ANRAs was compared with other CEs with CoS reported in the literature. Two kinds of CoS have been prepared and used as the catalyst on the CE of a DSSC in the literature. Wang *et al.* have prepared CoS film potentiostatically,[25] and Lin *et al.* have prepared honeycomb-like CoS film potentiodynamically;[39] these films were used as the CEs of DSSCs. The power conversion efficiency of the DSSC was 6.5% in the case of Wang *et al.* and was 6.01% in the case of Lin *et al.* In this study, an efficiency of 7.67% was achieved by using the CE with CoS ANRAs. Thus, the CE with CoS ANRAs renders a higher efficiency than the CEs with CoS reported in the literature. It is, however, to be noted that the substrates, electrolytes, and spacers in DSSCs are totally different in these three cases. As there is no perfectly comparable DSSC in the literature with the DSSC in this study, the two CEs with CoS mentioned above were prepared using the reported methods[25,39] and used in DSSCs, which were fabricated by the method used in this study. The power conversion efficiencies of these cells were compared. The photovoltaic parameters of these three cells are given in Table S1 in the Supporting Information. The table clearly shows that the cell using the CE with CoS ANRAs-24h performs better (η = 7.67%) than the other two cells (6.76 and 7.45%). Further results and detailed discussion on this matter are provided in the Supporting Information (Figures S4−S6 and Table S1).

CONCLUSIONS

Co_3O_4 acicular nanorod arrays (Co_3O_4 ANRAs) are completely converted to crystalline CoS ANRAs after a conversion period of 12 h. While the nanorods of Co_3O_4 are highly porous with tiny spherical or elliptical nanoparticles, the nanorods of CoS ANRAs-24h are in solid form with tiny nanoflakes on their surface. After 36 h of conversion, each nanorod shows several large and mosaic flower-like nanoflakes on its surface. XPS analysis indicates that CoSOH may be the major composition of these nanoflakes. The electrode with CoS ANRAs obtained after 24 h of conversion period (CoS ANRAs-24h) shows the highest electrocatalytic ability toward I^-/I_3^- among all of the electrodes. The electrode with CoS ANRAs-24h also shows a much better stability than sputtered Pt in I^-/I_3^- electrolyte. A power conversion efficiency of 7.67% is achieved for the DSSC with the CE with CoS ANRAs-24h, and this efficiency is nearly the same as that of the DSSC with sputtered Pt on its CE (7.70%).

METHODS

Chemicals. Cobalt chloride 6-hydrate (98%) was obtained from Showa Chemicals Inc., Japan. Urea (99.0%) and $LiClO_4$ (98%) were purchased from Sigma-Aldrich. Sodium sulfide 9-hydrate (ACS reagent, 98%) was purchased from Alfa Aesar. Anhydrous LiI, I_2, and acetonitrile (ACN) were purchased from Merck. 4-*tert*-Butylpyridine (TBP, 96%) and *tert*-butanol (TBA, 99.5%) were received from Acros. *cis*-Bis(isothiocyanato)bis-(2,2′-bipyridyl-4,4′-dicarboxylato) ruthenium(II)bis-tetrabutylammonium (N719) and 1,2-dimethyl-3-propylimidazolium iodide (DMPII) were obtained from Solaronix S.A., Aubonne, Switzerland. Ethanol (ACS reagent, 99.5%) was purchased from Aldrich Chemical Co. Two kinds of commercial TiO_2 pastes (Ti nanoxide T and Ti nanoxide R/SP) were purchased from Solaronix. All chemicals mentioned above were used as received. Deionized water (DIW) was used throughout the work.

Fabrication of the CoS ANRAs-CE. A thin film of Co_3O_4 ANRAs was obtained on an FTO glass substrate, first by using chemical bath deposition (CBD) followed by a pyrolysis treatment. In the CBD process, the FTO substrate (TEC-7, NSG America, Inc., New Jersey, USA, 7 Ω/□, with an exposed geometric area of 1.5 cm^2) was suspended upside-down in a closed bottle with an aqueous solution, containing 6.25 wt % of urea and 0.15 M of cobalt chloride, at 90 °C for 4 h. After the CBD process, the obtained film on the FTO was converted to the film of Co_3O_4 by pyrolyzing it at 400 °C for 30 min in air. The preparation method of Co_3O_4 ANRAs was reported in our previous work.[40,41] Thereafter, the obtained film of Co_3O_4 ANRAs on FTO was converted to CoS ANRAs by soaking it in a closed bottle containing 0.01 M Na_2S aqueous solution at 90 °C. Various periods (*i.e.*, 3 h, 12 h, 24 h, and 36 h) were used for the conversion process. After this conversion process, the obtained film was washed with DIW and dried at 60 °C; the CE with CoS ANRAs was thus obtained.

Sputtered Pt-CE, with a platinum thickness of 50 nm on FTO, was also prepared for comparison.

Fabrication of the DSSC. The commercial TiO_2 paste (Ti nanoxide T) was coated on a cleaned FTO substrate by doctor-blade method. The coated substrate was gradually heated to 450 °C (rate = 10 °C/min) in an oxygen atmosphere and subsequently sintered at that temperature for 30 min. After sintering the electrode at 450 °C and cooling it to room temperature, two layers of Ti nanoxide T and one layer of another TiO_2 paste (Ti nanoxide R/SP) were then coated on the electrode by doctor-blade method; the thus coated electrode was then sintered as in the previous process. The total thickness of the TiO_2 film was about 16 μm, which included 6 μm of the mentioned Ti nanoxide R/SP as the scattering layer on the top. A portion of 0.16 cm^2 was selected from the composite film as the active area by removing the side portions by scrapping. Thereafter, the electrode was dipped in a solution, containing 0.3 mM N719 dye in ACN/TBP (v/v = 1:1) for 18 h. The TiO_2 electrode was coupled with one of the various CEs (CEs with Co_3O_4 ANRAs, CoS ANRAs, and sputtered Pt) to fabricate the DSSC; these two electrodes were separated by a 60 μm thick Surlyn (Solaronix S.A., Aubonne, Switzerland) and sealed by heating. A mixture of 0.6 M DMPII, 0.125 M LiI, 0.045 M I_2, and 0.5 M TBP in ACN was used as the electrolyte. The electrolyte was injected into the gap between the two electrodes by capillarity, and the hole was sealed with hot-melt glue after the electrolyte injection.

Instrumentation. Cyclic voltammetric (CV) measurements were performed with a CHI 440 electrochemical workstation (CH Instruments, Inc., USA), using the conventional three-electrode system. One of the various CEs, a platinum sheet, and a Ag/Ag^+ electrode were used as the working electrode, counter electrode, and reference electrode, respectively. The solution of 10.0 mM LiI, 1.0 mM I_2, and 0.1 M $LiClO_4$ in ACN was used as the electrolyte for all CV measurements. CV curves were recorded at a scan rate of 50 mV/s. Tafel polarization curves were obtained using symmetrical cells, at 50 mV/s, using a CHI 440 instrument with a two-electrode system. The symmetrical cell contained two identical electrodes; the film area was confined to be 0.16 cm^2 by removing the side portions by scrapping. The two electrodes were separated by a 60 μm thick Surlyn. The electrolyte used for the symmetrical cells was the same as that used for the DSSCs. The assembled DSSCs were illuminated by a class A quality solar simulator (PEC-L11, AM1.5 G, Peccell Technologies, Inc.), and the incident light intensity (100 mW/cm^2) was calibrated with a standard Si cell (PECSI01, Peccell Technologies, Inc.). Electrochemical impedance spectra (EIS) were obtained by using a PGSTAT 30 potentiostat/galvanostat (Autolab, Eco-Chemie, The Netherlands), equipped with a FRA2 module, under a constant light illumination of 100 mW/cm^2. The frequency range explored was 60 kHz to 1.0 Hz. The applied bias voltage was set at the open-circuit voltage (V_{OC}) of the DSSC, between the CE and the FTO/TiO_2/dye electrode, starting from the short-circuit condition; the corresponding ac amplitude was 10 mV. The impedance spectra were analyzed by an equivalent circuit model. The morphologies of Co_3O_4 ANRAs and CoS ANRAs were observed by using scanning electron microscopy (SEM, Nova NanoSEM 230) and transmission electron microscopy (TEM, Hitachi H-7100, Japan). High-resolution transmission electron microscopy (HRTEM, Tecnai G2, 200 kV) was also employed to verify the crystalline compositions of the nanostructures of Co_3O_4 and CoS. Fast Fourier transform (FFT) was used to estimate the value of a lattice spacing from the HRTEM image. Energy-dispersive spectroscopic (EDS) mapping from TEM (JEOL JEM-2100) was also used for the elemental analysis of the nanorods of Co_3O_4 and CoS. The crystalline compositions of Co_3O_4 ANRAs and CoS ANRAs were verified by X-ray diffraction patterns (XRD, X-Pert, The Netherlands) with Cu Kα radiation. The thin films of Co_3O_4 ANRAs and CoS ANRAs were scraped from their substrates and dispersed each in 50 mL of ethanol to form the suspensions for UV−visible measurements. UV−visible spectrophotometry (UV−vis−NIR, V670, Jasco Co., Japan) was applied to obtain the UV−visible spectra of the suspensions. UV−vis diffuse reflectance spectra of the Co_3O_4 and CoS films were obtained by the same UV−visible spectrophotometer, equipped with an integral sphere. The surface compositions of the films were also verified by X-ray photoelectron spectroscopy (XPS, PHI 5000 VersaProbe system, ULVAC-PHI, Chigasaki, Japan), using a microfocused (100 μm, 25 W) Al X-ray beam, with a photoelectron take off angle of 45°. The Ar^+ ion source for XPS (FIG-5CE) was controlled by using a floating voltage of 0.2 kV. The binding energies obtained in the XPS analyses were corrected for specimen charging, by referencing the C 1s peak to 285 eV.

Conflict of Interest: The authors declare no competing financial interest.

Acknowledgment. This work was sponsored by the National Research Council of Taiwan. We would like to thank Dr. Chuan-Ming Tseng in the Institute of Physics, Academia Sinica, for the help with the EDS mapping.

Supporting Information Available: Additional experimental data and relative discussions. This material is available free of charge *via* the Internet at http://pubs.acs.org.

REFERENCES AND NOTES

1. Burda, C.; Chen, X.; Narayanan, R.; El-Sayed, M. A. Chemistry and Properties of Nanocrystals of Different Shapes. *Chem. Rev.* **2005**, *105*, 1025–1102.
2. Xia, Y. N.; Yang, P. D.; Sun, Y. G.; Wu, Y. Y.; Mayers, B.; Gates, B.; Yin, Y. D.; Kim, F.; Yan, Y. Q. One-Dimensional Nanostructures: Synthesis, Characterization, and Applications. *Adv. Mater.* **2003**, *125*, 353–389.
3. Rabin, O.; Herz, P. R.; Lin, Y. M.; Akinwande, A. I.; Cronin, S. B.; Dresselhaus, M. S. Formation of Thick Porous Anodic Alumina Films and Nanowire Arrays on Silicon Wafers and Glass. *Adv. Funct. Mater.* **2003**, *13*, 631–638.
4. Li, Y. G.; Tan, B.; Wu, Y. Y. Mesoporous Co_3O_4 Nanowire Arrays for Lithium Ion Batteries with High Capacity and Rate Capability. *Nano Lett.* **2008**, *8*, 265–270.
5. Chen, D.; Zhao, W.; Russell, T. P. P3HT Nanopillars for Organic Photovoltaic Devices Nanoimprinted by AAO Templates. *ACS Nano* **2012**, *6*, 1479–1485.
6. Li, Y.; Xu, D. S.; Zhang, Q. M.; Chen, D. P.; Huang, F. Z.; Xu, Y. J.; Guo, G. L.; Gu, Z. N. Preparation of Cadmium Sulfide Nanowire Arrays in Anodic Aluminum Oxide Templates. *Chem. Mater.* **1999**, *11*, 3433–3435.
7. Yue, G. H.; Yana, P. X.; Liu, J. Z.; Fan, X. Y.; Zhuo, R. F. Fabrication, Structure, Magnetic Properties of Highly Ordered Cobalt Disulfide Nanowire Arrays. *Appl. Phys. Lett.* **2005**, *87*, 262505.
8. Jha, H.; Schmidt-Stein, F.; Shrestha, N. K.; Kettering, M.; Hilger, I.; Schmuki, P. Formation of Magnetic Aluminium Oxyhydroxide Nanorods and Use for Hyperthermal Effects. *Nanotechnology* **2011**, *22*, 115601.
9. Döbbelin, M.; Tena-zaera, R.; Carrasco, P. M.; Sarasua, J.-R.; Cabañero, G.; Mecerreyes, D. Electrochemical Synthesis of Poly(3,4-ethylenedioxythiophene) Nanotube Arrays Using ZnO Templates. *J. Polym. Sci., Part A: Polym. Chem.* **2010**, *48*, 4648–4653.
10. Li, Y.; Wang, Z.; Ma, X. D.; Qian, X. F.; Yin, J.; Zhu, Z. K. Large-Scale CdX (X = S, Se) Microtube Arrays on Glass Substrate: Transformation of CdOHCl Microrod Arrays by a Simple Template-Sacrificing Solution Method. *J. Solid State Chem.* **2004**, *177*, 4386–4393.
11. Grange, P.; Delmon, B. The Role of Cobalt and Molybdenum Sulphides in Hydrodesulphurisation Catalysts: A Review. *J. Less-Common Met.* **1974**, *36*, 353–360.
12. Bao, S. J.; Li, C. M.; Guo, C. X.; Qiao, Y. Biomolecule-Assisted Synthesis of Cobalt Sulfide Nanowires for Application in Supercapacitors. *J. Power Sources* **2008**, *180*, 676–681.
13. Justin, P.; Ranga Rao, G. CoS Spheres for High-Rate Electrochemical Capacitive Energy Storage Application. *Int. J. Hydrogen Energy* **2010**, *35*, 9709–9715.
14. Yang, Z.; Chen, C. Y.; Chang, H. T. Supercapacitors Incorporating Hollow Cobalt Sulfide Hexagonal Nanosheets. *J. Power Sources* **2011**, *196*, 7874–7877.
15. Wang, Q.; Jiao, L.; Han, Y.; Du, H.; Peng, W.; Huan, Q.; Song, D.; Si, Y.; Wang, Y.; Yuan, H. CoS_2 Hollow Spheres: Fabrication

and Their Application in Lithium-Ion Batteries. *J. Phys. Chem. C* **2011**, *115*, 8300–8304.
16. Hu, Q. R.; Wang, S. L.; Zhang, Y.; Tang, W. H. Synthesis of Cobalt Sulfide Nanostructures by a Facile Solvothermal Growth Process. *J. Alloys Compd.* **2010**, *491*, 707–711.
17. Wang, Z.; Pan, L.; Hu, H.; Zhao, S. Co_9S_8 Nanotubes Synthesized on the Basis of Nanoscale Kirkendall Effect and Their Magnetic and Electrochemical Properties. *CrystEngComm* **2010**, *12*, 1899–1904.
18. Chen, X.; Zhang, Z.; Qiu, Z.; Shi, C.; Li, X. Hydrothermal Fabrication and Characterization of Polycrystalline Linneite (Co_3S_4) Nanotubes Based on the Kirkendall Effect. *J. Colloid Interface Sci.* **2007**, *308*, 271–275.
19. Yue, G. H.; Yan, P. X.; Fan, X. Y.; Wang, M. X.; Qu, D. M.; Wu, Z. G.; Li, C.; Yan, D. Structure and Properties of Cobalt Disulfide Nanowire Arrays Fabricated by Electrodeposition. *Electrochem. Solid-State Lett.* **2007**, *10*, D29–D31.
20. Oregan, B.; Grätzel, M. A Low-Cost, High-Efficiency Solar-Cell Based on Dye-Sensitized Colloidal TiO_2 Films. *Nature* **1991**, *353*, 737–740.
21. Mor, G. K.; Shankar, K.; Paulose, M.; Varghese, O. K.; Grimes, C. A. Use of Highly-Ordered TiO_2 Nanotube Arrays in Dye-Sensitized Solar Cells. *Nano Lett.* **2006**, *6*, 215–218.
22. Huang, Z.; Liu, X. H.; Li, K. X.; Li, D. M.; Luo, Y. H.; Li, H.; Song, W. B.; Chen, L. Q.; Meng, Q. B. Application of Carbon Materials as Counter Electrodes of Dye-Sensitized Solar Cells. *Electrochem. Commun.* **2007**, *9*, 596–598.
23. Roy-Mayhew, J. D.; Bozym, D. J.; Punckt, C.; Aksay, I. A. Functionalized Graphene as a Catalytic Counter Electrode in Dye-Sensitized Solar Cells. *ACS Nano* **2010**, *4*, 6203–6211.
24. Tai, Q. D.; Chen, B. L.; Guo, F.; Xu, S.; Hu, H.; Sebo, B.; Zhao, X. Z. *In Situ* Prepared Transparent Polyaniline Electrode and Its Application in Bifacial Dye-Sensitized Solar Cells. *ACS Nano* **2011**, *5*, 3795–3799.
25. Wang, M.; Anghel, A. M.; Marsan, B.; Ha, N.-L. C.; Pootrakulchote, N.; Zakeeruddin, S. M.; Grätzel, M. CoS Supersedes Pt as Efficient Electrocatalyst for Triiodide Reduction in Dye-Sensitized Solar Cells. *J. Am. Chem. Soc.* **2009**, *131*, 15976–15977.
26. Xu, R.; Zeng, H. C. Self-Generation of Tiered Surfactant Superstructures for One-Pot Synthesis of Co_3O_4 Nanocubes and Their Close- and Non-Close-Packed Organizations. *Langmuir* **2004**, *20*, 9780–9790.
27. Yang, J.; Liu, H. W.; Martens, W. N.; Frost, R. L. Synthesis and Characterization of Cobalt Hydroxide, Cobalt Oxyhydroxide, and Cobalt Oxide Nanodiscs. *J. Phys. Chem. C* **2010**, *114*, 111–119.
28. Schenck, C. V.; Dillard, J. G.; Murray, J. W. Surface-Analysis and the Adsorption of Co(II) on Goethite. *J. Colloid Interface Sci.* **1983**, *95*, 398–409.
29. Valiulienė, G.; Žieliene, A.; Vinkevičius, J. Investigation of the Interaction between Co Sulfide Coatings and Cu(I) Ions by Cyclic Voltammetry and XPS. *J. Solid State Electrochem.* **2002**, *6*, 396–402.
30. Bao, S. J.; Li, Y. B.; Li, C. M.; Bao, Q. L.; Lu, Q.; Guo, J. Shape Evolution and Magnetic Properties of Cobalt Sulfide. *Cryst. Growth Des.* **2008**, *8*, 3745–3749.
31. Baird, T.; Campbell, K. C.; Holliman, P. J.; Hoyle, R. W.; Huxam, M.; Stirling, D.; Williams, B. P.; Morris, M. Cobalt-Zinc Oxide Absorbents for Low Temperature Gas Desulfurization. *J. Mater. Chem.* **1999**, *9*, 599–605.
32. Loussot, C.; Afanasiev, P.; Vrinat, M.; Jobic, H.; Leverd, P. C. Amorphous Cobalt Oxysulfide as a Hydrogen Trap. *Chem. Mater.* **2006**, *18*, 5659–5668.
33. Bulatovic, S. M. *Handbook of Flotation Reagents: Chemistry, Theory and Practice: Flotation of Sulfide Ores*; Elsevier: Amsterdam, The Netherlands, 2007; pp 60−61.
34. Yoon, C. H.; Vittal, R.; Lee, J.; Chae, W. S.; Kim, K. J. Enhanced Performance of a Dye-Sensitized Solar Cell with an Electrodeposited-Platinum Counter Electrode. *Electrochim. Acta* **2008**, *53*, 2890–2896.
35. Wu, M. X.; Lin, X.; Wang, T. H.; Qiu, J. S.; Ma, T. L. Low-Cost Dye-Sensitized Solar Cell Based on Nine Kinds of Carbon Counter Electrodes. *Energy Environ. Sci.* **2011**, *4*, 2308–2315.
36. Bard, A. J.; Faulkner, L. R. *Electrochemical Methods: Fundamentals and Applications*, 2nd ed.; John Wiley & Sons, Inc.: New York, 2000; pp 103−104.
37. Olsen, E.; Hagen, G.; Lindquist, S. E. Dissolution of Platinum in Methoxy Propionitrile Containing LiI/I_2. *Sol. Energy Mater. Sol. Cells* **2000**, *63*, 267–273.
38. Lai, Y. H.; Lin, C. Y.; Chen, J. G.; Wang, C. C.; Huang, K. C.; Liu, K. Y.; Lin, K. F.; Lin, J. J.; Ho, K. C. Enhancing the Performance of Dye-Sensitized Solar Cells by Incorporating Nanomica in Gel Electrolytes. *Sol. Energy Mater. Sol. Cells* **2010**, *94*, 668–674.
39. Lin, J. Y.; Liao, J. H.; Wei, T. C. Honeycomb-like CoS Counter Electrodes for Transparent Dye-Sensitized Solar Cells. *Electrochem. Solid-State Lett.* **2011**, *14*, D41–D44.
40. Kung, C. W.; Lin, C. Y.; Lai, Y. H.; Vittal, R.; Ho, K. C. Cobalt Oxide Acicular Nanorods with High Sensitivity for the Non-Enzymatic Detection of Glucose. *Biosens. Bioelectron.* **2011**, *27*, 125–131.
41. Kung, C. W.; Lin, C. Y.; Li, T. J.; Vittal, R.; Ho, K. C. Synthesis of Co_3O_4 Thin Films by Chemical Bath Deposition in the Presence of Different Anions and Application to H_2O_2 Sensing. *Procedia Eng.* **2011**, *25*, 847–850.